Spectral Quadratic Variation Regularized Autoweighted Tensor Ring Decomposition for Hyperspectral Image Reconstruction

Xinwei Wan ⓘ, Dan Li ⓘ, Fanqiang Kong ⓘ, Yanyan Lv ⓘ, and Qiang Wang ⓘ, *Member, IEEE*

Abstract—The structure information of hyperspectral image (HSI) is well-characterized by tensors, surpassing the capabilities of traditional compressive sensing reconstruction models based on vectors and matrices. Tensor decomposition has been integrated with other regularizations in the model-based reconstruction algorithms to capture more priors. However, the existing tensor decomposition fails to achieve the best low-rank approximation. The effectiveness of model-based reconstruction methods can be promoted. In this article, a subspace-based model utilizing spectral quadratic variation regularized autoweighted tensor ring (TR) decomposition is proposed to explore the multiple-layer spatial–spectral priors of HSI. The original HSI is decomposed into the feature image and spectral basis to explore the first-layer spectral low-rankness. To capture the second-layer low-rank prior, TR decomposition is applied to obtain the effective low-rankness approximation and low computational complexity. The tensor nuclear norm is employed to describe underlying structure priors of the TR factors, which address the deficiency in tensor rank robustness and enhance the reconstruction quality. An autoweighted mechanism is utilized to account for the varying contributions of different TR factors to the low-rank approximation. Moreover, embedding spectral quadratic variation into subspace decomposition enhances spectral smoothness and continuity. Alternating minimization is used to optimize the spectral basis and feature HSI. Through comparative experiments on three datasets, the superiority of the proposed model is demonstrated.

Index Terms—Auto-weighted, compressive sensing (CS), hyperspectral image (HSI) reconstruction, spectral quadratic variation, tensor ring (TR) decomposition.

I. INTRODUCTION

COMPRESSIVE sensing (CS) [1], [2] holds that a signal, assumed to be compressible and sparse, can be reconstructed by fewer incoherent projection observations. Recently,

CS has been widely applied to the compression of hyperspectral image (HSI) [3], [4], [5], solving the dilemma of storing and transmitting the high-resolution HSI data. Various real implementations that adhere the restricted isometry property (RIP) [6] have been developed, including dual-camera compressive hyperspectral imaging [7] and the coded aperture snapshot spectral imager [8]. Original 3-D data cubes are downscaled and compressed into 2-D images or even 1-D signals. HSI compression uses the limited resources of spaceborne remote sensing for coding and shifting complex calculations to the ground decodeside. Hyperspectral image compressive sensing reconstruction (HSI-CSR) is theoretically solvable given the sparsity of HSI in certain transform domains. The critical challenge of HSI-CSR lies in proposing an effective reconstruction mechanism to improve the reconstruction quality since CS is an undetermined issue. CS reconstruction essentially involves solving for the minimum l_0 sparse term, which is an NP-hard problem and usually relaxed to the constrain of l_1 and l_p $(0 < p < 1)$ norm [6], [9]. Traditional model regularization methods based on sparse prior, such as sparse dictionary [10] and total variation (TV) norm [11], have been applied to HSI-CSR. Nonlocal means was incorporated in the spatial–spectral regularization to assume the global redundancy structure, enhancing the reconstruction results [12]. Wang et al. [13] proposed a method that combined l_1 spatial–spectral TV and l_0 gradient minimization to characterize the local structure information across all dimensions and enhance global smoothness. The proposed l_0-l_1 hybrid TV method addressed the oversmoothness of the TV norm and preserved the image edge information. Sparse regularization models consider the characteristics of HSI in both spatial and spectral domains and enable HSI-CSR. However, the reconstruction results are suboptimal and lose significant details as these methods fail to exploit additional priors such as significant low-rankness.

Assuming that the unfolding 2-D HSI exists low-rank prior, regularization models based on matrix low-rankness have been proposed [14], [15], [16]. These models face challenges in capturing the high-dimensional space information and achieving satisfactory reconstruction results at low sampling ratios. Moreover, the computational complexity increases with extensive unfolding data. Tensor is the most natural representation of high-dimensional data and has been successfully applied in computer

vision and pattern recognition [17], [18]. Tensor-based methods are effective in characterizing the complete structures and features of HSI. Low-rank tensor decomposition is broadly categorized into factorization-based methods and rank minimization-based methods [19]. Factorization-based methods, including CP decomposition and Tucker decomposition, have been widely employed in HSI-CSR. Das [20] applied Tucker decomposition in compressing HSIs and videos, improving the compression ratio and peak signal-to-noise ratio (PSNR). Since the simple low-rank tensor decomposition only leverages the low-rankness of partial dimensions, some studies have combined other inherent priors, such as sparsity and smoothness, to estimate additional space information. Joint tensor Tucker decomposition with a weighted 3DTV (JTenRe3-DTV) [21] combined Tucker decomposition with weighted 3DTV to simultaneously capture the low-rankness and the spatial–spectral correlation, which enhanced global smoothness and improved reconstruction results. The Tucker decomposition-based model encounters difficulty in achieving the perfect low-rank tensor and suffers from increased computational complexity with the exponential growth in the number of parameters relative to the data dimensionality. Meanwhile, the superposition of different regularizations ignores the low-rankness unfolding along different modes, including spectral and spatial domain and nonlocal stacking. To settle these challenges, subspace-based nonlocal tensor ring decomposition method (SNLTR) [22] integrated tensor ring (TR) decomposition [23], [24] into the subspace-based nonlocal similarity patch framework, capturing spectral low-rank prior and preserving global structural information. TR decomposition has been demonstrated to improve the reconstruction results of HSI-CSR compared with Tucker decomposition. The other type of tensor low-rank decomposition, rank minimization, is the NP-hard nonconvex problem. Tensor nuclear norm (TNN) [25], [26] is the convex surrogate of the nonconvex rank function. Fan et al. [27] formulated a low-rank tensor recovery model based on the tubal rank-related TNN to characterize the 3-D structural complexity of multilinear data. Global low-rank tensor optimization model with nonlocal plug-and-play regularizers (GNLR) [28] employed 3DTNN [29] to preserve the structural information of the original data in spatial and spectral domains, as the matrix factorization destroys the inherent structure of a third-order tensor. These two kinds of low-rank tensor decomposition have been combined in HSI missing data recovery. Total variation regularized weighted tensor ring decomposition (TVWTR) [30] analyzed the latent low-rank spaces of different TR cores to deeply explore the low-rank prior and applied variable weights for low-rank nuclear norms on the TR cores. Meanwhile, further exploration of the low-rankness and sparsity of the factors obtained from tensor decomposition improves the quality of tensor completion. MLSTD [31] proposed a multi-layer progressive regularization to explore the sparse prior of the HSI, which introduced gradient operation to capture the smoothness of the CP factor matrices and applied matrix factorization scheme to learn deeper layer structured sparsity. Zeng et al. [32] introduced a high-order low-rank decomposition into each mode of the underlying tensor based on Tucker decomposition and performed nonconvex relaxation on the low-rank submeasure to explore the multimode low-rank structure of tensors.

HSI data are redundant, and the significant information and image details remain in the low-rank subspace. The tensor decomposition-based regularization employed in the original tensor enhances the computational complexity and makes the HSI-CSR less efficient. Nonlocal meets global (NGMeet) [33] exploited nonlocal self-similarity in the low-rank feature HSI under subspace decomposition and reduced the computational complexity. Constraining the feature image to exploit the global and nonlocal properties promotes the effectiveness of HSI-CSR. Since subspace decomposition destroys the inherent 3-D data structure, other regularizations, including 3DTNN and 3DTV [34], [35], have been employed to constrain and exploit the characteristics of the original HSI. Subspace-based models have employed the semiorthogonal constraint in the spectral basis, which is inferred from mathematics and ignores the inherent priors in the spectral dimension. The continuous and generally smooth spectral feature of the HSI has been captured by using spectral–spatial TV in the underlying HSI [21], [36]. STCR [37] employed a difference continuity-regularization rather than the traditional semiorthogonal constraint to update the spectral basis and pursue the perfectly reconstructed HSI. In conclusion, the introduced methods completed the HSI-CSR and obtained the passable reconstructed results while ignoring the global structure of HSI and failing to explore the inherent low-rank prior of different modes and the smoothness of the HSI.

In this work, we propose a HSI-CSR model combining spectral quadratic variation with auto-weighted TR (SQV-AwTR) cores nuclear norm minimization. The model guarantees the smoothness of the spectrum and explores the multiple-layer low-rank prior, which ensures a more accurate approximation of the TR rank. First, the original HSI is decomposed into a subspace considering the spectral low-rank prior. As the feature HSI is updated, the spectral bands gradually increases and the low-rank features become more obvious. TR decomposition is then applied to constrain the obtained feature HSI, which inherits the low-rank prior, to improve the reconstruction efficiency. Subsequently, to effectively highlight the low-rankness of TR cores, the autoweighted (TNN) is proposed to thoroughly explore the spatial–spectral structural information and the low-rank prior of the feature tensor. It is based on convex relaxation by penalizing the weighted sum of the nuclear norm of TR cores. As for the spectral basis, the band-neighboring pixels in the spectral vector have smooth continuity in the spectrum. Finally, the spectral quadratic variation is introduced to constrain it instead of orthogonal constraints.

1) We propose a subspace-based reconstruction model to characterize the spectral smoothness and multiple-layer low-rankness, which explores the spatial–spectral priors of the tensor decomposition factors layer by layer.
2) We apply the spectral quadratic variation instead of the orthogonal constraint to update the spectral basis and enhance the smooth continuity of the spectral dimension, improving the reconstructed results.

3) We utilize autoweighted TNN to further exploit the strength of the low-rank prior of different TR cores, making the model robust to selecting TR ranks. Meanwhile, the autoweighted mechanism avoids the omission of manual assignment.

The rest of this article is organized as follows. Section II describes some notations and corresponding definitions. The proposed model and the optimization procedure are presented in Section III. Section IV illustrates the experimental results and evaluates the proposed and comparing models. Finally, Section V concludes this article.

II. RELATED WORK

A. Citation

We use x, $\boldsymbol{x}$, and $\mathbf{X}$ for scalars, vectors, and matrices. An n-order tensor is defined as $\mathcal{X} \in \mathbb{R}^{I_1 \times I_2 \times \cdots \times I_n}$ by calligraphic letters, and the 3-D HSI cube is represented as $\mathcal{X} \in \mathbb{R}^{m \times n \times s}$. The ith frontal (mode-3) slice of the cube is represented as $\mathcal{X}_{::i}$, equivalent to the MATLAB operation $\mathcal{X}(:,:,i)$. The Frobenius norm of the HSI cube is defined as $\|\mathcal{X}\|_F = (\sum_{m_i,n_i,s_i} |\mathcal{X}_{m_i,n_i,s_i}|^2)^{1/2}$, where the element value of the position (m_i, n_i, s_i) is represented as $\mathcal{X}_{m_i,n_i,s_i}$. Through the article, two types of mode-k unfolding of the tensor $\mathcal{Z}$ in the size $I_1 \times I_2 \times \cdots \times I_n$ are introduced. The traditional mode-k matricization [38] is defined as $\mathbf{Z}_{(k)} \in \mathbb{R}^{I_k \times I_1 \cdots I_{k-1} I_{k+1} \cdots I_n}$, and the corresponding folding tensor is represented as $\text{fold}(\mathbf{Z}_{(k)}, k)$. An unconventional tensor-matrix product employing the mode-n unfolding has been wildly applied in tensor decomposition defined as $\times_n$. $\mathcal{Z} \times_n \mathbf{B}$ is equivalent to $\text{fold}n(\mathbf{B}\mathbf{Z}_{(n)})$ under this calculation, where the matrix $\mathbf{B}$ is in the size of $B_n \times I_n$. In TR decomposition [23], a new mode mode-k unfolding is represented as $\mathbf{Z}_{\langle k \rangle} \in \mathbb{R}^{I_k I_{k+1} \cdots I_n I_1 \cdots I_{k-1}}$ and there exists the matrix folding similarly.

B. Definitions

Definition 1 (Spectral quadratic variation [39], [40]): In the context of tensor completion, the penalty term $\|\mathbf{V}\boldsymbol{e}_r\|_p^p$ based on minimizing the nonsmoothness measure, is employed to capture the smoothness prior of the feature vectors $\boldsymbol{e}_r$ and induce the spectral smoothness of the tensor, where

$$\mathbf{V} = \begin{bmatrix} 1 & -1 & & \\ & 1 & -1 & \\ & & \ddots & \ddots \\ & & & 1 & -1 \end{bmatrix}. \tag{1}$$

The regularization takes the form of TV and quadratic variation when $p = 1$ and $p = 2$, respectively. An essential application of the spectral quadratic variation is evident in the reconstruction of the spectral basis, due to the continuous nature of the individual vector of the latent spectral basis and the smoothness of the spectrum.

Definition 2 (TR Decomposition [23], [41]): TR decomposition of an n-dimensional tensor $\mathcal{Z}$ is a cyclic interconnection of multiple cube data, known as TR factors (or core tensors) $\mathcal{R}^N = \{\mathcal{R}^1, \mathcal{R}^2, \ldots, \mathcal{R}^n\}$. It can be viewed as the linear combination

of the tensor train (TT) decomposition [42], which settles the problem of obtaining the optimal solution of TT decomposition. The latent tensor $\mathcal{R}^k$ is in the size of $r_k \times I_k \times r_{k+1}$, where $r_1 = r_{n+1}$ due to the trace operation. $\boldsymbol{r} = [r_1, r_2, \ldots, r_n]^T$ is referred to as TR rank. The elementwise relationship of TR decomposition is represented as

$$\mathcal{Z}_{i_1,i_2,\ldots,i_n} = \text{Tr}\left(\prod_{k=1}^{n} \mathbf{R}^k(i_k)\right) \tag{2}$$

in which $\text{Tr}(\cdot)$ is the trace operation of $\mathbf{R}^k(i_k)$, the i_kth lateral slice of TR factor $\mathcal{R}^k$. TR decomposition is the circular multilinear products over the latent three-order tensors. Defining $[\mathcal{R}]$ as the multiply of n TR cores, TR decomposition can be denoted by the operator Φ as

$$\mathcal{Z} = \Phi([\mathcal{R}]). \tag{3}$$

Definition 3 (TNN [25]): TNN is defined as a norm, adding up all singular values of the frontal slice of $\hat{\mathcal{X}}$ (the fast Fourier transformation of $\mathcal{X}$ along the spatial domain). It can be calculated as

$$\|\mathcal{X}\|_{TNN} = \sum_{i=1}^{s} \left\|\hat{\mathcal{X}}_{::i}\right\|_*. \tag{4}$$

The matrix nuclear norm $\|\cdot\|_*$ denotes the sum of the singular values and constrains the low-rankness.

C. Weighted TR Decomposition

TR decomposition has been employed for recovering high-dimensional images for its superior ability to characterize low-rankness [43], [44]. However, a significant drawback is finding an optimal solution, as the number of model possibilities extends exponentially with the dimensionality of the data. TRLRF model [45] for tensor completion employed nuclear norms in the unfolding core tensors and is formulated as

$$\min_{\mathcal{Z},[\mathcal{R}]} \frac{\lambda}{2} \|\mathcal{Z} - \Phi([\mathcal{R}])\|_F^2 + \sum_{n=1}^{N} \sum_{i=1}^{3} \left\|\mathbf{R}_{(i)}^n\right\|_*. \tag{5}$$

The model minimized the fitting error of the tensor low-rank approximation and nuclear norms simultaneously to reduce the complexity of setting the TR rank. Wang et al. [30] examined the low-rank properties of three core tensors obtained by TR decomposition of the HSI. The research focused on investigating their singular value distribution curves after mode-n unfolding and concluded that mode-2 unfolding exhibits a stronger low-rank correlation. Different weights were designed as $[\alpha_1, \alpha_2, \alpha_3] = [1, \alpha, 1]/(2 + \alpha)$ to reflect the relative importance of matrix nuclear norms of the three TR latent tensors. In addition, the weighted TR decomposition solves the problem of tensor rank initialization and enhances the robustness of the decomposition model. ATRFHS [46] applied an autoweighted mechanism [47] to represent the contribution of all latent tensor cores to low-rankness. This model combined TV and phase congruency regularization with weighted TR decomposition, effectively characterizing low-rank and sparse priors and retaining clear edge information to restore the noising HSI. Moreover,
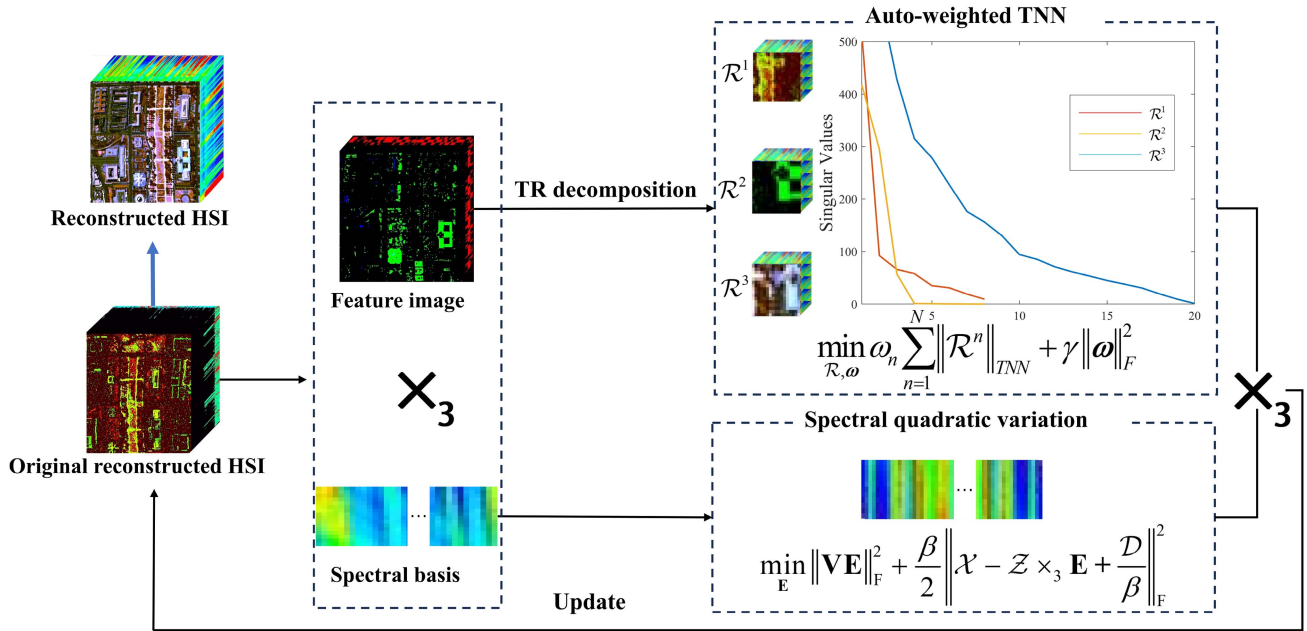
Fig. 1. Flowchart of the proposed SQV-AwTR decomposition model.

Xu et al. [48] compared the hyperspectral–multispectral image fusion quality with different norms constraints on TR cores. They found that TNN achieved the highest PSNR values than matrix nuclear norms and TR without constraint. TNN is more effective in preserving the intrinsic structure information of TR cores.

III. PROPOSED MODEL AND ALGORITHM

A. Proposed Model for HSI Reconstruction

The proposed HSI-CSR model SQV-AwTR combines spectral quadratic variation and autoweighted TR decomposition in a unified framework and is illustrated in Fig. 1. The original reconstructed HSI is obtained from the simple SVD or DCT operation and has the redundancy. It is decomposed into the subspace (feature image) $\mathcal{Z}$ to capture more features and reduce the computational complexity. The regular orthogonal constraint for the spectral basis $\mathbf{E}$ is discarded. The spectral quadratic variation represented as $\|\mathbf{VE}\|_F^2$ is applied to enhance the smoothness and spectral continuity of HSI. TR decomposition is employed to characterize the prior knowledge since the feature tensor inherits the global low-rankness. As the feature HSI is updated, the spectral bands gradually increases and the low-rank features become more obvious. Previous experiments have demonstrated that imposing different constraints on the TR factors has varying effects on reconstruction results, with the TNN constraint providing the most significant improvement in PSNR values. In Fig. 1, the singular value distribution curves for the three latent tensors illustrate the low-rankness of TR factors. To represent the different contributions of each core to low-rank priors, an autoweighted strategy is applied in the TNN constraining latent cores. The autoweighted TNN leads to better low-rank approximation and makes the setting of the TR ranks more feasible and robust. Moreover, the autoweighted

strategy learns the weights ω_n of TNN values of three factors, compensating for the deficiency of manual assignment. Gathering the above-mentioned regularization terms into the unified framework, the proposed SQV-AwTR model captures the low-rank prior and enhances the spectral smoothness. The model is formulated as

$$\min_{\mathcal{X},\mathbf{E},\mathcal{Z},\mathcal{R},\boldsymbol{\omega}} \frac{1}{2}\|\boldsymbol{y}-\Psi(\mathcal{X})\|_F^2 + \lambda_1\|\mathbf{VE}\|_F^2 + \lambda_2\|\mathcal{Z}-\Phi([\mathcal{R}])\|_F^2$$

$$+ \sum_{n=1}^{N} \omega_n \left\|\mathcal{R}^{(n)}\right\|_{\text{TNN}} + \gamma\|\boldsymbol{\omega}\|_F^2$$

$$\text{s.t.} \mathcal{X} = \mathcal{Z}\times_3\mathbf{E}, \boldsymbol{\omega}^T 1 = 1, \boldsymbol{\omega} \geq 0 \quad (6)$$

where λ and γ are the regularization parameters to balance the fidelity and regularization terms, $\boldsymbol{y}$ is the CS observation, and $\Psi(\cdot)$ is the CS operator for tensor.

1) Spectral Smoothing Subspace Model for HSI-CSR: CS is an efficient method for HSI compression. The high-dimensional HSI $\mathcal{X} \in \mathbb{R}^{m\times m\times s}$, with the spatial resolution $m \times n$ and s bands, is mapped to a low-dimensional observation $\boldsymbol{y} \in \mathbb{R}^M$. The CS operator Ψ represents the simultaneous process of compressed and sampling. In addition to some realistic hyperspectral compressive imaging systems, Ψ is realized by the operator $\mathbf{D} \cdot \mathbf{F} \cdot \mathbf{P}$, which combines random downsampling, random permutation and the Fourier transform (denoted by $\mathbf{D}$, $\mathbf{F}$, and $\mathbf{P}$, respectively). It has been demonstrated that Ψ satisfies the RIP, making the HSI-CSR problem theoretically solvable. To address the ill-posed inverse problem, various priors have been applied as the regularizations $P(\mathcal{X})$ in the CS reconstruction model. The HSI-CSR model is denoted as

$$\min_{\mathcal{X}} \frac{1}{2}\|\boldsymbol{y} - \Psi(\mathcal{X})\|_F^2 + \lambda P(\mathcal{X}) \quad (7)$$

where the parameter λ is used for balancing the fidelity and regularization terms.

The direct application of HSI-CSR to the massive original HSI data leads to computational inefficiency due to the redundant information. Potential feature HSI mapped in subspace inherits the structure and the properties of the initial tensor, such as low-rankness and nonlocal priors. Consequently, incorporating regularizations in the feature HSI, rather than the original HSI, improves the reconstruction efficiency. The model (7) can be rewritten as

$$\min_{\mathcal{X},\mathcal{Z},\mathbf{E}} \frac{1}{2} \|\boldsymbol{y} - \Psi(\mathcal{X})\|_F^2 + \lambda P(\mathcal{Z})$$
$$\text{s.t.} \mathcal{X} = \mathcal{Z} \times_3 \mathbf{E}, \mathbf{E}^T \mathbf{E} = \mathbf{I} \tag{8}$$

where $\mathcal{Z}$ in the size of $m \times n \times k$ is the feature image, and $\mathbf{E} \in \mathbb{R}^{s \times k}(k \ll s)$ is the spectral basis.

The afore-mentioned mode-n tensor-matrix decomposition considers the low-rank prior of the spectral domain. However, the simple orthogonally constraint on the spectral base ignores the spectral continuity and smoothness inherent in HSI. The band-neighboring pixels in the spectral vector have smooth continuity in the spectrum. Spectral quadratic variation is introduced to update $\mathbf{E}$ and capture more spectral priors. Each column of $\mathbf{E}$ mathematically combines to form the spectral vectors of the original HSI. Quadratic variation increases smoothness and continuity of the spectral basis, thereby improving the smooth continuity of HSI in the spectral domain. In each iteration, the feature HSI $\mathcal{Z}$ and spectral basis $\mathbf{E}$ crossing the high dimensions are reprojected into the high-dimensional space, which improves reconstruction results. The spectral smoothing subspace model for HSI-CSR is denoted as follows:

$$\min_{\mathcal{X},\mathcal{Z},\mathbf{E}} \frac{1}{2} \|\boldsymbol{y} - \Psi(\mathcal{X})\|_F^2 + \lambda_1 \|\mathbf{V}\mathbf{E}\|_F^2 + \lambda_2 P(\mathcal{Z})$$
$$\text{s.t.} \mathcal{X} = \mathcal{Z} \times_3 \mathbf{E}. \tag{9}$$

2) Autoweighted TR Decomposition: Due to its ability to provide the best low-rank approximation, TR decomposition has been widely applied in HSI processing, including HSI-CSR, missing data recovery, and HSI denoising. TR decomposition without constraints obtains poor reconstruction results compared with applying matrix and tensor constraints. TNN is incorporated into the TR factors to enable the preservation of 3-D structural features and a deeper exploration of the low-rank prior of kernel tensors, which improves reconstruction quality. The model combined TNN and TR decomposition is defined as

$$\min_{\mathcal{Z},\mathcal{R}} \frac{1}{2} \|\mathcal{Z} - \Phi([\mathcal{R}])\|_F^2 + \sum_{n=1}^{N} \omega \left\| \mathcal{R}^{(n)} \right\|_{\text{TNN}}. \tag{10}$$

The optimization process of the model ensures the robustness of the TR rank setting. Examination of the singular values distribution curves highlights the differences in the low-rank characteristics of the three core tensors. Different weights are assigned to the TNN to characterize different contributions of TR factors to the low-rank approximation. Manual assignments of these weights are deemed crude and uncritical, prompting the

introduction of an autoweighted mechanism, defined as

$$\min_{\boldsymbol{\omega}} \sum_{n=1}^{N} \omega \left\| \mathcal{R}^{(n)} \right\|_{\text{TNN}} + \gamma \|\boldsymbol{\omega}\|_F^2$$
$$\text{s.t.} \boldsymbol{\omega}^T \mathbf{1} = 1, \boldsymbol{\omega} \geq 0 \tag{11}$$

where $\boldsymbol{\omega}$ symbolizes the self-learning weights. The autoweighted strategy has been applied in TR decomposition and TT decomposition to make the assignment mechanism more flexible and reliable. The autoweighted TR decomposition can be denoted as

$$\min_{\mathcal{Z},\mathcal{R},\boldsymbol{\omega}} \frac{1}{2} \|\mathcal{Z} - \Phi([\mathcal{R}])\|_F^2 + \sum_{n=1}^{N} \omega_n \left\| \mathcal{R}^{(n)} \right\|_{\text{TNN}} + \gamma \|\boldsymbol{\omega}\|_F^2$$
$$\text{s.t.} \boldsymbol{\omega}^T 1 = 1, \boldsymbol{\omega} \geq 0. \tag{12}$$

B. Optimization Procedure

Alternating optimization is applied to efficiently find the solution for model (6). The proposed model is optimized in two parts, subspace decomposition, and autoweighted TR decomposition, which are detailed as follows.

1) Subproblem of Autoweighted TR Decomposition: Fix the variables associated with subspace decomposition to solve for TR factors. The subproblem of TR decomposition with TNN can be denoted as

$$\min_{\mathcal{R},\mathcal{G}} \frac{1}{2} \|\mathcal{Z} - \Phi([\mathcal{R}])\|_F^2 + \sum_{n=1}^{N} \omega_n \left\| \mathcal{G}^{(n)} \right\|_{\text{TNN}}$$
$$\text{s.t.} \mathcal{G}^{(n)} = \mathcal{R}^{(n)}. \tag{13}$$

Once the TR factors are determined, the weighted can be derived

$$\min_{\boldsymbol{\omega}} \sum_{n=1}^{N} \omega_n \left\| \mathcal{G}^{(n)} \right\|_{\text{TNN}} + \gamma \|\boldsymbol{\omega}\|_F^2$$
$$\text{s.t.} \boldsymbol{\omega}^T 1 = 1, \boldsymbol{\omega} \geq 0. \tag{14}$$

The augmented Lagrangian equation of model (13) based on the ADMM algorithm is written as

$$\min_{\mathcal{R},\mathcal{G}} \frac{1}{2} \|\mathcal{Z} - \Phi([\mathcal{R}])\|_F^2 + \sum_{n=1}^{N} \omega_n \left\| \mathcal{G}^{(n)} \right\|_{\text{TNN}}$$
$$+ \frac{\beta_1}{2} \sum_{n=1}^{N} \left\| \mathcal{G}^{(n)} - \mathcal{R}^{(n)} + \frac{\mathcal{D}_1^{(n)}}{\beta_1} \right\|_F^2 \tag{15}$$

where β_1 is the ADMM penalty parameter, and $\mathcal{D}_1$ is the Lagrangian multiplier. The optimization of this equation is performed in three steps as follows.

1) Update $\mathcal{R}$ on the TR decomposition

$$\hat{\mathcal{R}} = \underset{\mathcal{R}}{\arg\min} \frac{1}{2} \|\mathcal{Z} - \Phi(\mathcal{R})\|_F^2$$
$$+ \frac{\beta_1}{2} \sum_{n=1}^{N} \left\| \mathcal{G}^{(n)} - \mathcal{R}^{(n)} + \frac{\mathcal{D}_1^{(n)}}{\beta_1} \right\|_F^2. \tag{16}$$

Based on circular dimensional permutation invariance, each TR factor can rank first in the chain. TR decomposition $\mathcal{Z} = \Phi([\mathcal{R}])$ is calculated as $\mathbf{Z}_{\langle 2 \rangle} = \mathbf{R}_{\langle 2 \rangle}^{(k)}(\mathbf{R}_{\langle 2 \rangle}^{(k \neq 2)})^T$. The least-squares problem (16) is solved as follows:

$$\mathcal{R}^{(n)} = \text{fold2}\left(\left(\mathbf{Z}_{\langle n \rangle} \mathbf{R}_{\langle 2 \rangle}^{(\neq n)} + \beta_1 \mathbf{G}_{(2)}^{(n)} + \mathbf{D}_{1(2)}^{(n)} \right) \right.$$
$$\left. \left(\mathbf{R}_{\langle 2 \rangle}^{(\neq n),T} \mathbf{R}_{\langle 2 \rangle}^{(\neq n)} + \beta_1 \mathbf{I} \right)^{-1} \right). \quad (17)$$

2) Update $\mathcal{G}^{(n)}$ on the TNN

$$\hat{\mathcal{G}}^{(n)} = \underset{\mathcal{G}^{(n)}}{\arg \min} \, \omega_n \left\| \mathcal{G}^{(n)} \right\|_{\text{TNN}}$$
$$+ \frac{\beta_1}{2} \sum_{n=1}^{N} \left\| \mathcal{G}^{(n)} - \mathcal{R}^{(n)} + \frac{\mathcal{D}_1^{(n)}}{\beta_1} \right\|_F^2. \quad (18)$$

The core of the optimization is to solve the proximal operator. The operator tensor singular value thresholding [26] is defined to obtain the closed-form and formulated as

$$\text{SVT}_\tau(\mathcal{X}) = \mathcal{U} * \mathcal{S}_\tau * \mathcal{V}^* \quad (19)$$

where the factorization $\mathcal{U} * \mathcal{S} * \mathcal{V}^*$ is tensor-SVD. $\mathcal{S}_\tau = \text{ifft}((\text{fft}(\mathcal{S}, [\ ], 3) - \tau)_+, [\ ], 3)$, in which $\text{fft}(\mathcal{S}, [\ ], n)$, $\text{ifft}(\mathcal{S}, [\ ], n)$ denotes to the fast Fourier transform and the inverse transform in the n-th dimension. The soft threshold is embodied in $st_+ = \max(st, 0)$. The subproblem according to TNN is updated as

$$\mathcal{G}^{(n)} = \text{SVT}_{\frac{1}{\omega_n}}\left(\mathcal{R}^{(n)} - \frac{\mathcal{D}_1^{(n)}}{\beta_1} \right). \quad (20)$$

3) Update the multiplier $\mathcal{D}_1$ by

$$\mathcal{D}_1^{(n)} = \mathcal{D}_1^{(n)} + \beta_1(\mathcal{G}^{(n)} - \mathcal{G}^{(n)}). \quad (21)$$

The block coordinate descent algorithm is applied to optimize the autoweighted subproblem (14) once the TNN values are determined. The Lagrangian function of this quadratic optimization problem is formulated as

$$L(\boldsymbol{\omega}, \boldsymbol{\sigma}, \mu) = \boldsymbol{\eta}^T \boldsymbol{\omega} + \gamma \|\boldsymbol{\omega}\|_F^2 - \mu(\boldsymbol{\omega}^T 1 - 1) - \boldsymbol{\sigma}^T \boldsymbol{\omega} \quad (22)$$

where μ and $\boldsymbol{\sigma}$ is the Lagrangian multiplier, and $\boldsymbol{\eta} = [\|\mathcal{G}^{(1)}\|_{\text{TNN}}, \|\mathcal{G}^{(2)}\|_{\text{TNN}}, \|\mathcal{G}^{(3)}\|_{\text{TNN}}]^T$. The weights ω_n is

$$\omega_n = \frac{\sigma_n + \mu - \eta_n}{2\gamma}. \quad (23)$$

Since the optimal solution should confirm to the KKT condition [47], ω_n is calculated as

$$\omega_n = \begin{cases} \frac{\mu - \eta_n}{2\gamma}, n \leq M \\ 0, n > M \end{cases}, \mu = \frac{\sum\limits_{n=1}^{M} \eta_n + 2\gamma}{M} \quad (24)$$

where $M = \text{argmax}_n((\mu - \eta_n) > 0)$.

2) Subproblem of Subspace Optimization: TR factors $\mathcal{G}$ and corresponding weights ω_n have been fixed, and the subproblem can be rewritten as

$$\min_{\mathcal{X}, \mathbf{E}, \mathcal{Z}} \frac{1}{2} \|y - \Psi(\mathcal{X})\|_F^2 + \lambda_1 \|\mathbf{VE}\|_F^2 + \lambda_2 \|\mathcal{Z} - \Phi([\mathcal{R}])\|_F^2$$
$$\text{s.t.} \mathcal{X} = \mathcal{Z} \times_3 \mathbf{E}. \quad (25)$$

The nonconvex problem is optimized by the ADMM algorithm, and the augmented Lagrangian function can be denoted as

$$\min_{\mathcal{X}, \mathcal{Z}, \mathbf{E}} \frac{1}{2} \|\boldsymbol{y} - \Psi(\mathcal{X})\|_F^2 + \lambda_1 \|\mathbf{VE}\|_F^2 + \lambda_2 \|\mathcal{Z} - \Phi([\mathcal{R}])\|_F^2$$
$$+ \frac{\beta_2}{2} \left\| \mathcal{X} - \mathcal{Z} \times_3 \mathbf{E} + \frac{\mathcal{D}_2}{\beta_2} \right\|_F^2 \quad (26)$$

where β_2 is the ADMM penalty parameter, and $\mathcal{D}_2$ is the Lagrangian multiplier. The next step is to optimize $\mathcal{X}$, $\mathcal{Z}$, $\mathbf{E}$, respectively.

1) The $\mathcal{X}$-subproblem is given by

$$\hat{\mathcal{X}} = \underset{\mathcal{X}}{\arg \min} \frac{1}{2} \|\boldsymbol{y} - \Psi(\mathcal{X})\|_F^2$$
$$+ \frac{\beta_2}{2} \left\| \mathcal{X} - \mathcal{Z} \times_3 \mathbf{E} + \frac{\mathcal{D}_2}{\beta_2} \right\|_F^2. \quad (27)$$

Preconditioned conjugated gradient can solve the quadratic optimization problem, and the equation can be denoted as

$$(\Psi^* \Psi + \beta_2) \mathcal{X} = \Psi^* y + \beta_2 \mathcal{Z} \times_3 \mathbf{E} - \mathcal{D}_2 \quad (28)$$

in which Ψ^* is the adjoint of Ψ.

2) The $\mathcal{Z}$-subproblem is given by

$$\hat{\mathcal{Z}} = \underset{\mathcal{Z}}{\arg \min} \lambda_2 \|\mathcal{Z} - \Phi([\mathcal{R}])\|_F^2$$
$$+ \frac{\beta_2}{2} \left\| \mathcal{X} - \mathcal{Z} \times_3 \mathbf{E} + \frac{\mathcal{D}_2}{\beta_2} \right\|_F^2. \quad (29)$$

By solving the tensor-form equation as follows, the closed-form solution is obtained:

$$(2\lambda_2 + \beta_2) \mathcal{Z} = 2\lambda_2 \Phi([\mathcal{R}]) + \beta_2 \left(\mathcal{Z} + \frac{\mathcal{D}_2}{\beta_2} \right) \times_3 \mathbf{E}^T. \quad (30)$$

3) The $\mathbf{E}$-subproblem is given by

$$\hat{\mathbf{E}} = \underset{\mathbf{E}}{\arg \min} \lambda_1 \|\mathbf{VE}\|_F^2$$
$$+ \frac{\beta_2}{2} \left\| \mathcal{X} - \mathcal{Z} \times_3 \mathbf{E} + \frac{\mathcal{D}_2}{\beta_2} \right\|_F^2. \quad (31)$$

When setting the deviation to zero, the equation is equivalent to

$$\frac{2\lambda_1}{\beta_2} \mathbf{V}^T \mathbf{VE} + \mathbf{EZ}_{(3)}(\mathbf{Z}_{(3)})^T = \left(\mathbf{X}_{(3)} + \frac{\mathbf{D}_{1(3)}}{\beta_2} \right)(\mathbf{Z}_{(3)})^T \quad (32)$$

Algorithm 1: SQV-AwTR for HSI Reconstruction.

Require: sampling operator Ψ, compressive measure vector $\boldsymbol{y}$.

1: Initialize: $\mathcal{X}^*$ (DCT), subspace spectral bands k^0, feature
   HSI $\mathcal{Z}$ and spectral basis $\mathbf{E}$.
2: **for** $j = 1 : J$ **do**
3:    Update $k^j = \min\{s, k^{j-1} + \delta * (i - 1)\}$.
4:    Estimate $\mathcal{Z}$ and $\mathbf{E}$ from the SVD of $\mathcal{X}^*$.
5:    Update $\mathcal{R}^{(n)}, \mathcal{G}^{(n)}$ by (17) and (20), respectively.
6:    Update weights ω_n by (24).
7:    **While** $\frac{\|\mathcal{X}^{t+1} - \mathcal{X}^t\|_F}{\|\mathcal{X}^t\|_F} > \varepsilon$ **do**
8:       Update $\mathcal{X}$ by (28).
9:       Update $\mathcal{Z}$ by (30).
10:       Update $\mathbf{E}$ by (32).
11:       Update multiplier $\mathcal{D}_2$ by (33).
12:    **end while**
13:    Update HSI: $\mathcal{X}^* = \mathcal{Z} \times_3 \mathbf{E}$.
14: **end for**
Output: $\mathcal{X}^*$.

which is the Sylvester matrix equation in the form of $\mathbf{C}_1 \mathbf{A} + \mathbf{A} \mathbf{C}_1 = \mathbf{C}_3$ and solved by Bartels–Stewart method commonly [49].

4) The multiplier $\mathcal{D}_2$ is updated by

$$\mathcal{D}_2 = \mathcal{D}_2 + \beta_2(\mathcal{X} - \mathcal{Z} \times_3 \mathbf{E}). \tag{33}$$

Algorithm 1 concludes the optimization procedure of the proposed SQV-AwTR method. k^0 is estimated by HySime [50], and $\mathbf{E}$ is estimated using SVD.

C. Computational Complexity

The computational complexity of the SQV-AwTR model is analyzed in this section. The HSI in the assumed size $I \times I \times I$ is discussed for convenience. Similarly, the TR rank is assumed to be $\boldsymbol{r} = [r, r, r]^T$. TR decomposition and the per-iteration of updating TNN with the theoretically highest computational complexity take about $\mathcal{O}(3r^2I^3 + 3r^6)$ and $\mathcal{O}(r^3 \log r + r^4)$, respectively. In addition, updating subproblems according to subspace decomposition take about $\mathcal{O}(I^3)$ time each. In conclusion, the total computation cost of the proposed SQV-AwTR method for CS reconstruction is $\mathcal{O}(N(3r^2I^3 + 3r^6 + r^3 \log r + r^4 + n(I^3)))$, in which n is the ADMM iteration times, and N is the times for updating subspace.

IV. NUMERICAL EXPERIMENTS

A. Experimental Setup

To evaluate the effectiveness of the proposed SQV-AwTR algorithm in HSI-CSR, experiments are conducted on three widely used HSI datasets under five sampling ratios (sr). Related experiments are carried out on MATLAB R2019b and a laptop with an Intel Core i7 CPU at 2.80 GHz.

1) Dataset: To demonstrate the robustness and effectiveness of the proposed algorithm, three widely used HSI datasets

TABLE I
DATASETS IN EXPERIMENTS AND THEIR DETAILS

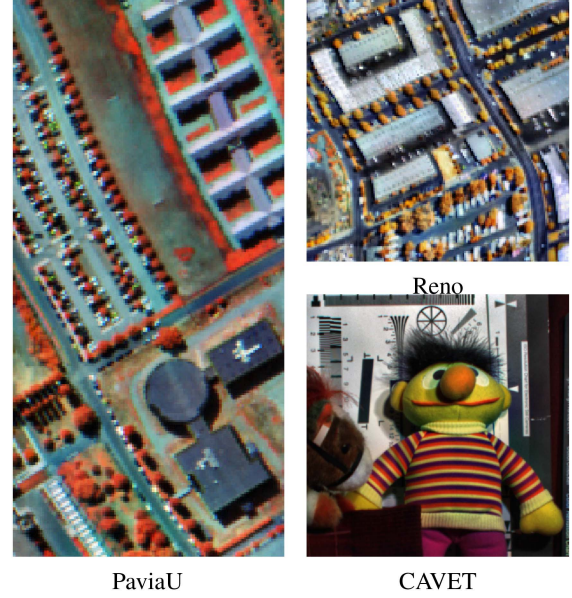| Dataset	Spatial resolution	Spectral bands
PaviaU	250×121	103
Reno	150×150	100
CAVET	300×300	31

Fig. 2. RGB images of the PaviaU dataset, the Reno dataset, and the CAVET dataset.

with varying spatial features and spectral band numbers are selected for experiments, including the Pavia University (PaviaU) datasets, the Reno dataset, and the CAVE Toy (CAVET) dataset. These HSIs are cropped to facilitate the experiments. The specific details of datasets are listed in Table I. In addition, the RGB images are presented in Fig. 2 for visual reference.

2) Parameters Setting: It is crucial to determine the variable regularization parameters, ADMM penalty parameters, and TR ranks to achieve the best reconstruction results of the SQV-AwTR algorithm at all datasets under all sampling ratios. In the experiments, regularization parameters λ_1, λ_1, γ are all uniformly set to 1 on three datasets at all ratios. Meanwhile, β_1 and β_2 are set to $\beta_1 = 1e - 3$, and $\beta_2 = 1$, respectively. The TR ranks are set to $[9, 3, 3]^T$. Apart from these analytically adjusted parameters, the other parameters are more robust and can be set based on experience and previous experiments. The parameter δ, which updates the spectral bands, is set to 2 according to Hysime [50]. The TR decomposition parameter ρ is set to 1 according to He et al.'s [41] work. The parameters of the comparison models are set by referencing the published papers and codes to ensure optimal experimental data.

3) Comparison Algorithms: Six methods are employed for comparing, including DCT, TV-regularized low-rank matrix factorization (LRTV) [51], JTenRe3-DTV [21], $l_0 - l_1$HTV [13], GNLR [28], and NGMeet [33]. All the comparison algorithms apply the same compression operator as the proposed SQV-AwTR model. DCT is used to compute the initialization of the proposed algorithm. $l_0 - l_1$HTV is the most recent state-of-the-art method. LRTV and JTenRe3-DTV integrate low-rank

TABLE II
QUANTITATIVE RESULTS FOR EXPERIMENTAL MODELS OF THREE DATASETS AT ALL SAMPLING RATIOS

Dataset	Ratios	Index	DCT	LRTV	JTenRe3-DTV	$l_0 - l_1$HTV	GNLR	NGMeet	SQV-AwTR
PaviaU	0.02	PSNR	24.591	23.255	29.020	23.319	24.949	29.521	**31.600**
		SSIM	0.6062	0.6560	0.8115	0.6443	0.7195	0.8464	**0.8558**
		ERGAS	221.51	270.58	132.53	260.51	181.20	125.27	**100.47**
	0.05	PSNR	27.393	29.746	32.407	29.148	28.756	35.007	**38.542**
		SSIM	0.7571	0.8874	0.9054	0.8558	0.8535	0.9422	**0.9551**
		ERGAS	160.77	129.96	91.15	132.16	116.93	67.86	**46.49**
	0.1	PSNR	30.875	39.539	33.789	35.392	31.933	38.862	**43.765**
		SSIM	0.8748	0.9736	0.9254	0.9412	0.9179	0.9703	**0.9860**
		ERGAS	108.24	46.06	78.67	66.42	81.20	44.98	**25.59**
	0.15	PSNR	33.560	42.588	34.723	38.392	35.189	44.978	**46.341**
		SSIM	0.9231	0.9820	0.9360	0.9626	0.9566	0.9771	**0.9924**
		ERGAS	79.96	35.75	71.27	48.36	55.91	34.26	**18.88**
	0.2	PSNR	36.847	44.550	35.910	40.434	37.900	45.783	**49.174**
		SSIM	0.9392	0.9848	0.9478	0.9720	0.9749	0.9860	**0.9960**
		ERGAS	63.814	30.63	63.09	39.71	40.98	26.72	**13.74**
Reno	0.02	PSNR	22.350	20.248	27.656	19.145	27.795	28.985	**32.160**
		SSIM	0.5782	0.5992	0.8027	0.5510	0.7622	0.8512	**0.9031**
		ERGAS	245.80	320.46	134.35	356.92	152.58	114.16	**81.68**
	0.05	PSNR	25.846	26.567	32.443	25.126	31.842	34.530	**41.712**
		SSIM	0.7554	0.8576	0.9236	0.8015	0.8849	0.9584	**0.9853**
		ERGAS	163.34	155.50	78.12	178.23	96.33	60.50	**27.98**
	0.1	PSNR	29.246	38.263	35.811	31.878	35.127	42.652	**44.221**
		SSIM	0.8686	0.9815	0.9621	0.9269	0.9385	0.9916	**0.9919**
		ERGAS	111.03	43.87	54.35	82.61	65.77	24.52	**20.63**
	0.15	PSNR	31.795	41.440	37.770	35.808	38.355	46.990	**46.992**
		SSIM	0.9196	0.9887	0.9746	0.9633	0.9664	0.9950	**0.9953**
		ERGAS	82.88	31.59	44.76	53.19	46.03	17.42	**17.20**
	0.2	PSNR	34.122	43.429	38.957	38.576	41.730	49.749	**49.835**
		SSIM	0.9490	0.9916	0.9800	0.9780	0.9829	0.9957	**0.9968**
		ERGAS	63.50	25.92	39.68	38.89	31.33	14.44	**12.82**
CAVET	0.02	PSNR	24.130	14.429	27.695	22.245	27.940	25.779	**31.067**
		SSIM	0.6419	0.2861	0.8163	0.5371	0.7644	0.7229	**0.8346**
		ERGAS	214.89	657.03	145.20	263.12	137.77	175.47	**116.27**
	0.05	PSNR	27.559	16.493	32.713	22.698	32.729	33.791	**34.896**
		SSIM	0.7928	0.3384	0.9130	0.5613	0.8776	0.9426	**0.9465**
		ERGAS	149.73	523.58	91.40	249.65	80.50	69.86	**65.45**
	0.1	PSNR	31.040	19.565	35.046	30.935	34.324	40.208	**40.984**
		SSIM	0.8655	0.4371	0.9328	0.8595	0.8974	**0.9779**	0.9614
		ERGAS	102.15	373.18	75.45	97.19	67.46	33.32	**32.45**
	0.15	PSNR	33.273	22.896	36.314	35.097	36.221	41.858	**42.389**
		SSIM	0.9013	0.5579	0.9340	0.9456	0.9030	**0.9819**	0.9749
		ERGAS	73.38	257.32	70.50	54.11	61.96	27.54	**26.36**
	0.2	PSNR	36.180	27.059	37.849	40.243	36.946	45.193	**46.467**
		SSIM	0.9217	0.7088	0.9543	0.9737	0.9254	0.9909	**0.9917**
		ERGAS	63.69	161.80	54.24	34.56	50.48	18.75	**16.43**

priors and TV norms, while the former is based on matrix decomposition and the latter on tensor decomposition. NGMeet model and GNLR model are based on low-rank subspace.

4) Evaluation Indicators: The quality of the reconstruction algorithms is assessed mainly in terms of visual effects and quantitative indices. The numerical indicators are image quality evaluation indices including structural similarity (SSIM), PSNR, erreur relative globale adimensionnelle de synthese (ERGAS), and Times, which indicates the HSI-CSR efficiency of the model. The image quality is evaluated in spatial and spectral dimensions, respectively. PSNR and SSIM values characterize the spatial information. The larger the values, the better the reconstruction result. ERGAS values represent the spectral distortion, and small ERGAS values reflect the complete spectral structure.

B. Experimental Results

1) Quantitative Analysis of Results: Table II lists the reconstruction results of all the compared methods at all sampling ratios under the PaviaU, Reno, and CAVET datasets. The optimal evaluation indicators are indicated in bold,

demonstrating that the proposed SQV-AwTR method achieves the best reconstruction results overall. DCT, a traditional 2-D CS reconstruction method, experiences difficulty in completing the HSI-CSR task, particularly at small sampling ratios. The LRTV and the JTenRe3-DTV method incorporate local smoothness with low-rank decomposition. The former reconstruction results are better at high sampling ratios (above 0.05) but incomplete at low sampling ratios on the PaviaU and Reno datasets, while the latter obtains the opposite trend. Moreover, the reconstruction results of LRTV on the CAVET dataset are the worst in all cases since the PSNR values are all below 30 dB, reflecting a lack of stability in the two competitive methods. $l_0 - l_1$HTV, combined with the l_0 norm and l_1 norm, promotes global spectral–spatial smoothness and performs well at sampling rates higher than 0.05. It focuses on the sparse prior and ignores the low-rankness, which incompletes recovery of the spatial information and decreases PSNR and SSIM values at small sampling rates, particularly in the CAVET dataset. Subspace-based methods, including NGMeet, GNLR, and the proposed model, achieve better reconstruction results in the evaluation indicators of spatial
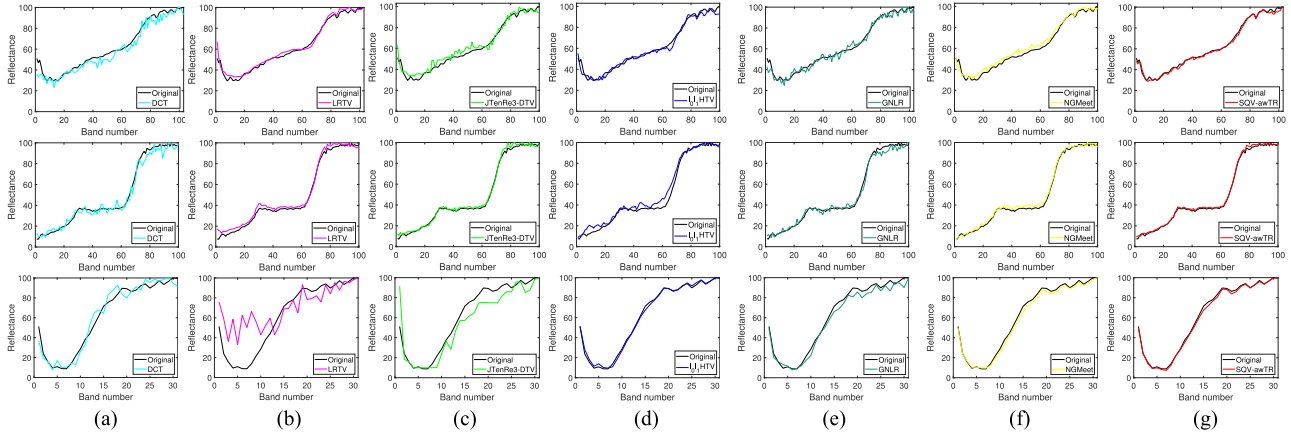
Fig. 3. Spectrum signatures of pixels of original and reconstruction HSIs in the sampling ratios sr=0.15. The first row: on the PaviaU dataset of pixel (120,80). The second row: on the Reno dataset of the pixel (90,75). The third row: on the CAVET dataset of pixel (150,150). (a) DCT. (b) LRTV. (c) JTenRe3DTV. (d) $l_0 - l_1$HTV. (e) GNLR. (f) NGmeet. (g) SQV-AwTR.

and spectral dimensions. Subspace decomposition captures spectral low-rankness and the constrained feature image captures more effective prior information. SQV-AwTR model significantly improves the reconstruction results for the PaviaU and Reno datasets with hundreds of bands, surpassing the suboptimal NGMeet algorithm by at least 3 dB in PSNR values, especially at sampling ratios smaller than 0.15. Autoweighted TR decomposition fully exploits the low-rank priors and guarantees the reconstruction results in the spatial domain with limited observations on complex 3-D images. NGMeet employs similarity patches to obtain nonlocal similarity of feature images and attains improved structural information in datasets with small spectral dimensions. Meanwhile, the datasets with low spectral dimensionality lack spectral correlation and spectral low-rankness, leading to insignificant improvement in the reconstruction accuracy of our method. The enhancement effect of our method is not apparent and fails to reach the highest SSIM values at 0.1 and 0.15 sampling ratios under the CAVET dataset. GNLR combines more regularizations to capture nonlocal self-similarity, low-rankness, and sparsity, while the reconstruction results are poor, indicating that more regular terms are not better, and a suitable combination is necessary. GNLR integrates 3DTNN on the original image to preserve the structural information. Our method constrains the TR factors of the feature images with TNN, which better characterizes the low-rankness information of the 3-D image and improves the reconstruction results. The proposed SQV-AwTR model obtains the smallest ERGAS values and guarantees more spectral signatures in all comparative experiments. It indicates that the spectral quadratic variation constraining on the spectral basis reduces the spectral distortion and enhances the spectral reconstruction results.

Since the ERGAS values do not vary much at high sampling ratios, the spectral feature curves are plotted to visualize the spectral fidelity of the reconstruction HSI. Fig. 3 plots the spectral profiles of pixels in the reconstruction and original HSIs at a sampling ratio of 0.15 for all three datasets. The more similar the spectral profile is to the original profile, the lower the spectral

distortion and the better the reconstruction. LRTV model lacks the most spectral information on the CAVET datasets, demonstrating its instability in reconstructing datasets with different spectrum features. As shown in Fig. 3, the subspace-based models constrain the feature image and simultaneous updates of the spectral basis, resulting in a more complete spectral structure in the reconstruction HSI. The difference between the ERGAS values of our method and NGMeet is less than 1 on the Reno and the CAVET datasets. The spectral feature curves of the proposed SQV-AwTR method better fit the original curves, as depicted in Fig. 3(f) and (g), which reflects that the model preserves more spectral signatures because the spectral quadratic variation guarantees the spectral continuity and smoothness. Moreover, Fig. 4 presents the PSNR charts for all bands on three datasets at low and high sampling ratios (sr=0.05 and sr=0.15) to analyze the robustness of comparative algorithms. SQV-AwTR achieves the highest PSNR values in the vast majority of bands for all datasets, with particularly significant improvements at small sampling ratios, demonstrating the robustness and superiority of our reconstruction algorithm.

To analyze the algorithmic computational efficiency, the average reconstruction time for all the methods in the comparison experiments for each dataset is plotted in the bar charts shown in Fig. 5. DCT is the fastest as a traditional CS reconstruction algorithm but unsuitable for 3-D data. JTenRe3-DTV utilizes the tensor low-rank decomposition rather than the matrix low-rank property in combination with 3DTV, increasing the computational complexity. Meanwhile, it achieves considerably better reconstruction results than LRTV at small sampling ratios. $l_0 - l_1$HTV obtains decent computational efficiency and mediocre reconstruction results by applying simple regularization and considering only sparsity and smoothness. Subspace decomposition has advantages and disadvantages, with the outer loop updating the feature image increasing the time cost but the reconstruction quality being much higher. GNLR and the proposed method both employ TNN with about the same running time, but our methods improve the PSNR values by about 9 db on average. Compared to NGMeet, the TR decomposition
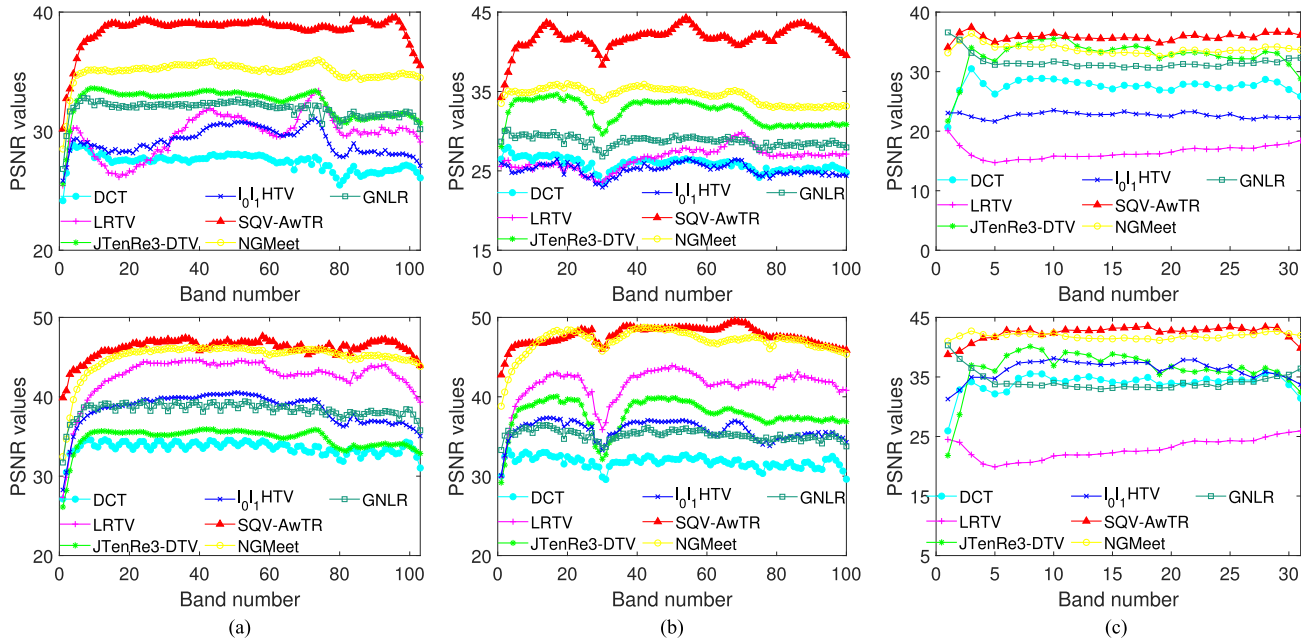
Fig. 4.   PSNR values of each band of competing models on three datasets at two ratios. Top row: sr=0.05. Bottom row: sr=0.15. (a) PaviaU. (b) Reno. (c) CAVET.
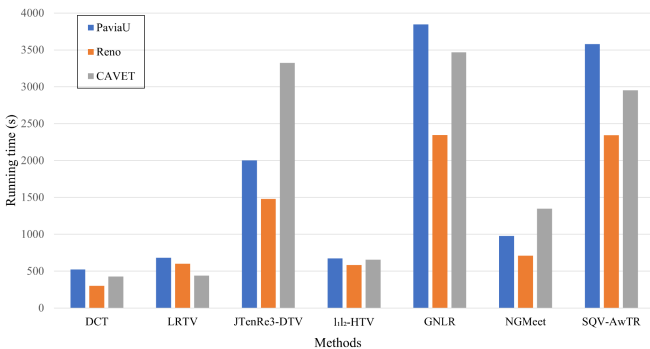

Fig. 5.   Average running times of all methods for HSI-CSR on all datasets.

subproblem solving in our algorithm takes much time, but it is worthwhile for the best reconstruction results are obtained.

2) Visual Results: The visual results of the reconstructed HSIs are mainly compared in the form of false-color images to observe their structural integrity and edge information, and details are compared by zooming in on the frame. Meanwhile, for RGB images of competing methods indistinguishable from eyes, error images between original and reconstructed HSIs are employed to demonstrate visual superiority further. Figs. 6–8 represent the RGB images synthesized by selecting three bands from HSIs in the first row and the error images on all datasets under the sampling ratio sr=0.1 in the second row. The color of error image changes from blue to yellow, indicating an increasing difference. LRTV fails to reconstruct compressive HSI on the CAVET datasets shown in Fig. 8(a), reflecting that integrating TV norms in the matrix low-rank frameworks cannot cope with the complex texture information and is too unstable for wide application. Except for this case, the comparison

models successfully reconstruct the basic image structure on all datasets. DCT loses the street details from Figs. 6(a) and 7(a), and the reconstructed HSI is fuzzy on the CAVET dataset. TV regularization recovers some edge and texture information but causes oversmoothing, as shown in Fig. 7(b)–(d). LRTV, JTenRe3-DTV, and $l_0 - l_1$HTV neglect to restore the aligned black dots in the blue box. In contrast, subspace-based methods reconstruct the main features of the HSIs and achieve better reconstruction results, showing the effectiveness of capturing the priors of feature HSI. Compared with GNLR, the zoom boxes of $l_0 - l_1$HTV display the missing details. Single sparse regularization is worse than the combination of multiple regularizations and results in blurring the reconstructed images and spoiling the details. Meanwhile, the reconstructed images of GNLR contain artifacts and show a difference in color and contrast compared to the original image, especially on the CAVET dataset. The proposed model and the MGMeet model obtain the best RGB reconstructed images. Error images are employed to evaluate the HSI-CSR quality. As shown in Fig. 7(f) and (g), the error images of NGMeet and the proposed SQV-AwTR have a small portion of larger errors on the right side. Subspace-based methods fail to obtain sufficient low-rank prior and details from the black images in the Reno dataset. While there exists a small part of unsatisfactory results in the error image, the overall reconstruction results of the proposed method are the best and the same as the quantitative results. From (f) and (g) in Figs. 6 and 8, the blue portions in the error images of our method are more heavily weighted and darker in color, verifying that the proposed SQV-AwTR model achieves the best reconstruction results visually.

In summary, the proposed SQV-AwTR achieves superior reconstructed results in quantitative indicators and visualization on the three datasets with distinct spatial structures and
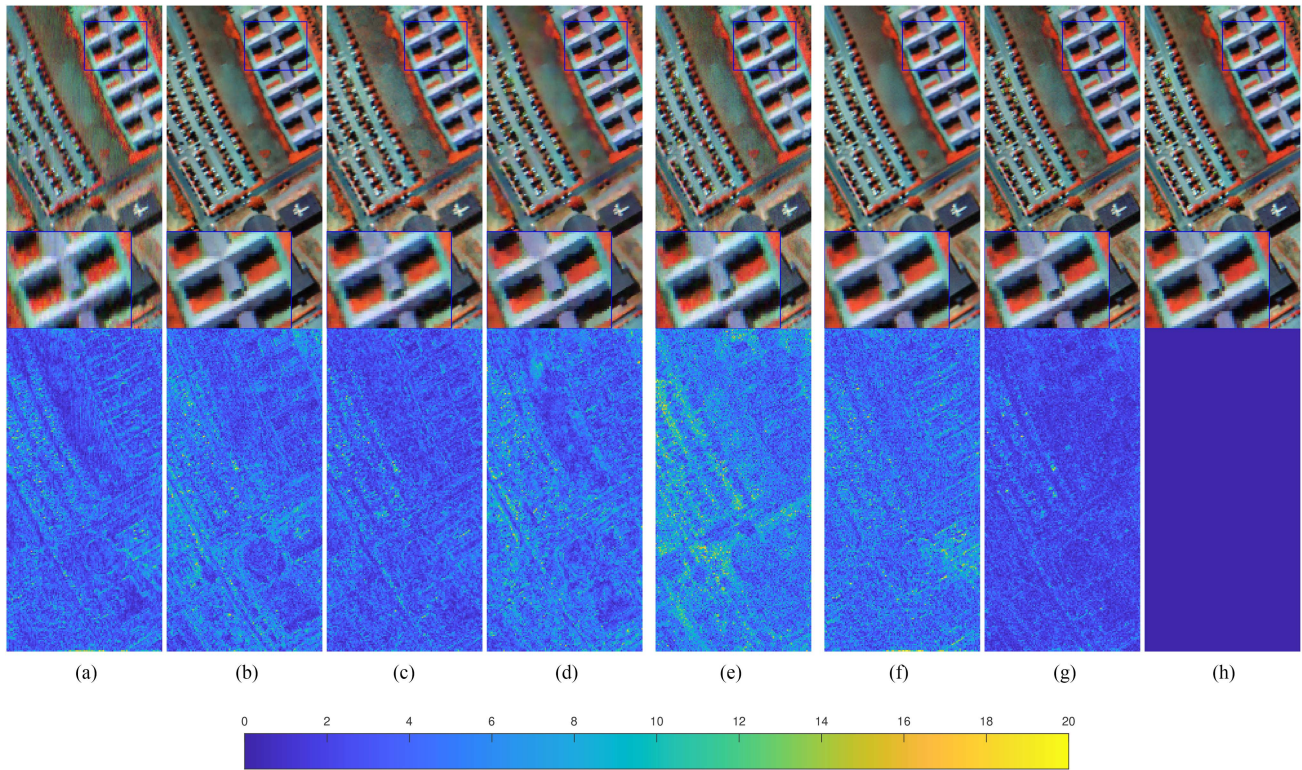
Fig. 6. Reconstructed HSIs on the PaviaU dataset when the sampling ratio is 0.1. Top: RGB images (selected bands: 100, 70, 40). Bottom: error images. (a) DCT. (b) LRTV. (c) JTenRe3-DTV. (d) $l_0 - l_1$HTV. (e) GNLR. (f) NGMeet. (g) SQV-AwTR. (h) Original.
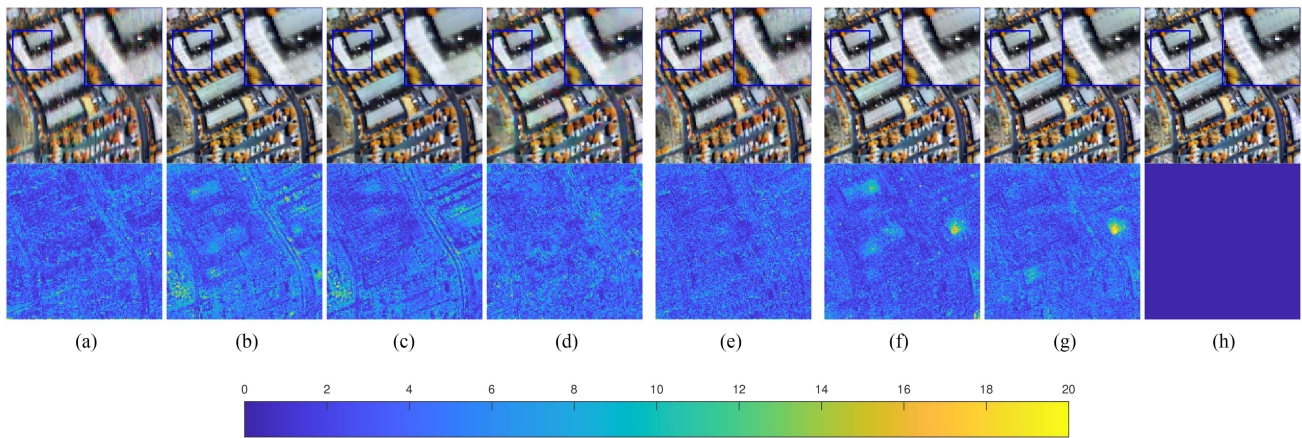

Fig. 7. Reconstructed HSIs on the Reno dataset when the sampling ratio is 0.1. Top: RGB images (selected bands: 100,70,35). Bottom: error images (a) DCT. (b) LRTV. (c) JTenRe3-DTV. (d) $l_0 - l_1$HTV. (e) GNLR. (f) NGMeet. (g) SQV-AwTR. (h) Original.

spectrum under five sampling ratios. Our algorithm improves the general subspace-based model by employing the spectral quadratic variation to enhance the spectral smooth continuity and fidelity while decreasing the EARGAS values. The promotion afforded by SQV-AwTR is more significant at low sampling ratios (smaller than 0.1) compared with other models, which verifies that autoweighted TR decomposition obtains better low-rank approximation and reconstruction results with fewer observations. NGMeet achieves the highest SSIM values on the CAVET dataset at the sampling ratios sr = 0.1 and 0.15.

On the one hand, self-similarity is an excellent property to capture the structure information. On the other, datasets with fewer bands fail to provide global correlation and subsequently impact the TR decomposition. Autoweighted TNN employed in TR factors captures more low-rankness than constrains the original HSI. Thus, the proposed SQV-AwTR completes the shortcomings of GNLR. Constraining the spectral basis and feature images and updating them simultaneously captures more priors and contributes to the superiority of the proposed model.
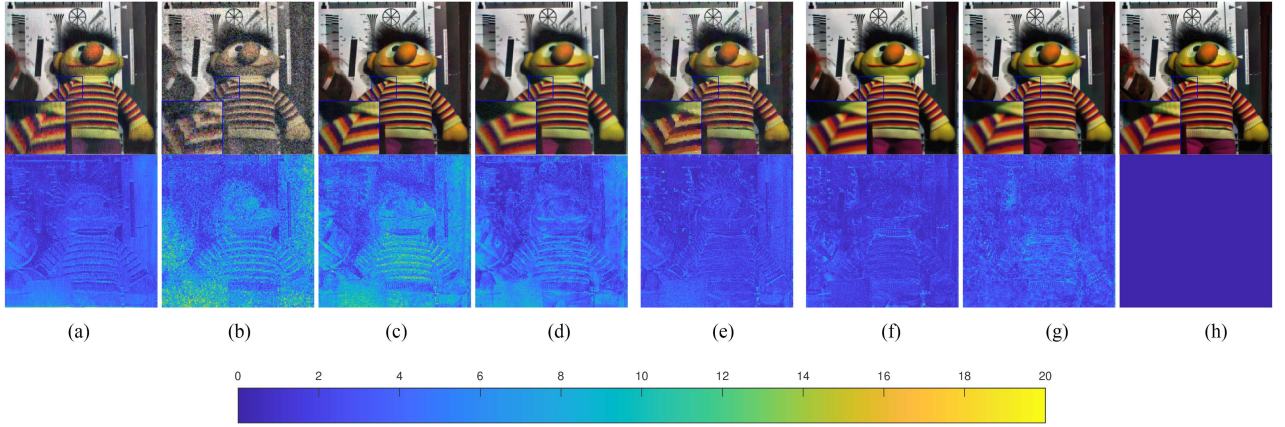
Fig. 8.   Reconstructed HSIs on the CAVET dataset when the sampling ratio is 0.1. Top: RGB images (selected bands: 31, 20, 10). Bottom: error images. (a) DCT. (b) LRTV. (c) JTenRe3-DTV. (d) $l_0 - l_1$HTV. (e) GNLR. (f) NGMeet. (g) SQV-AwTR. (h) Original.
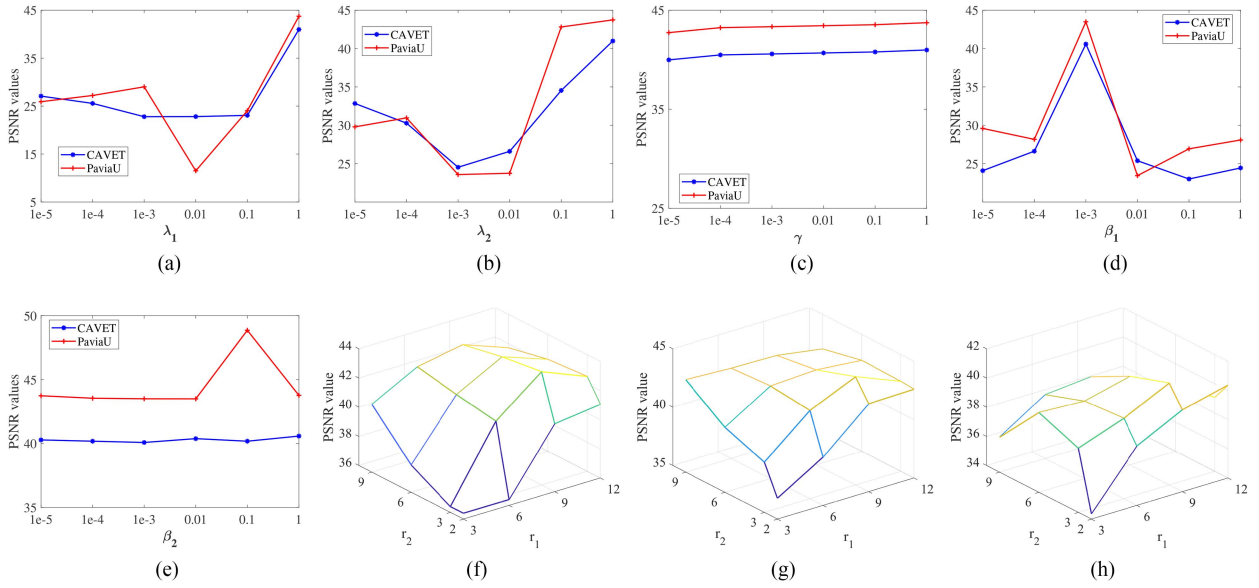

Fig. 9.   PSNR values variation with different parameter valued when $sr = 0.1$ on different datasets. (a) λ_1. (b) λ_2. (c) γ. (d) β_1. (e) β_2. (f) r (PaviaU). (g) r (Reno). (h) r (CAVET).
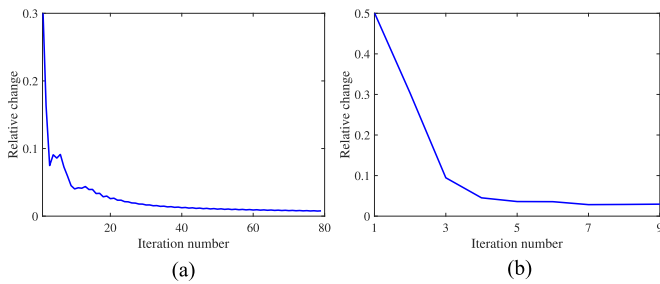

Fig. 10.   Numerical analysis of algorithm convergence. (a) Inner iteration. (b) Outer iteration.

C. Discussion

1) Ablation Study: The proposed SQV-AwTR model for HSI-CSR incorporates the autoweighted TNN on TR factors and spectral quadratic variation instead of the orthogonal constraint to update the spectral basis, improving the reconstruction results. Ablation experiments are performed at a small sampling ratio (sr=0.05) on all datasets to demonstrate the contribution of each regularization to the reconstruction and the plausibility of their combination. As Table III shows, the proposed method achieved the best reconstruction on all evaluation indicators, highlighted in bold. First, the difference between applying the traditional constraint (TR), TV norm (TRTV), and quadratic variation (TRQV) on the spectral basis is compared when performing the same TR decomposition on feature images. TRTV and TRQV obtain better reconstructions, especially with significantly lower ERGAS values on the PaviaU and Reno datasets, which have more spectral bands. Quadratic variation has a stronger convexity than TV, and TRQV performs well compared with TRTV in low sampling ratio under all datasets. Spectral quadratic

TABLE III
QUANTITATIVE RESULTS OF ABLATION STUDY UNDER ALL DATASETS WHEN
THE SAMPLING RATIO IS 0.05

Dataset	Index	TR	TRTV	TRQV	TRTNN-QV	SQV-AwTR
PaviaU	PSNR	23.999	25.915	26.485	37.508	**38.542**
	SSIM	0.5484	0.6316	0.6941	0.9449	**0.9551**
	ERGAS	236.45	189.65	189.52	51.88	**46.49**
Reno	PSNR	21.289	23.320	24.451	40.580	**41.712**
	SSIM	0.4894	0.6073	0.6114	0.9815	**0.9853**
	ERGAS	277.01	218.68	215.90	31.33	**27.98**
CAVET	PSNR	24.004	26.226	26.878	31.648	**34.896**
	SSIM	0.5576	0.5319	0.6500	0.9014	**0.9465**
	ERGAS	214.72	197.96	194.68	69.46	**65.45**

variation effectively characterizes the spectral smoothing and continuity of the original HSI. Then, the second-best reconstruction results are obtained by imposing TNN constraints on the TR factors based on TRQV (TRTNN-QV). The experiments presented in Section II demonstrate that applying tensor constraints on the core tensors works better than matrix constraints or no constraints for low-rankness. TNN enhances the exploitation of the low-rankness of the feature HSI and substantially improves the reconstruction results when the observations are limited. Finally, SQV-AwTR incorporates a self-weighting mechanism to characterize the contribution of different kernels to the low-rank approximation and intelligently adjusts the weights of the TNN regularizations to obtain better reconstruction results. The ablation experiments are layered to demonstrate the rationale and superiority of the proposed SQV-AwTR algorithm.

2) Parameters Influence: We analyze the setting of the critical parameters in the reconstruction algorithm, including regularization parameters λ_1, λ_2, γ, ADMM penalty parameters β_1, β_2, and TR ranks r. The effect of different parameter settings on the reconstruction results is compared by PSNR values at a sampling ratio of 0.1. The parameters λ_1, λ_2, γ, β_1, and β_2 are analyzed on the PaviaU and CAVET datasets with significant differences in spectral dimensions. The impact of TR ranks r on the reconstruction results is compared on all three datasets to verify the robustness of the TR ranks settings.

1) *Regularization parameters* λ, γ: The regularization parameters indicate the weight of different constraints to balance the fidelity and regularization terms. As shown in Fig. 9(a)–(c), parameters from the range [1e-5, 1e-4, 1e-3, 0.01, 0.1, 1] are selected for comparison experiments. When λ_1 and λ_2 are less than 1, the PSNR values are low, and there is a qualitative leap in the reconstruction results when they are equal to 1. Fig. 9(c) shows that the values of γ minimally impact the reconstruction results. The regularization parameters are set as $\lambda_1 = 1$, $\lambda_2 = 1$, $\gamma = 1$ for all datasets and sampling ratios based on the variation curves.

2) *ADMM penalty parameters* β: ADMM penalty parameters range from [1e-5, 1e-4, 1e-3, 0.01, 0.1, 1]. Fig. 9(d) and (e) plots the pattern of variation of PSNR values with parameter values. The PSNR value initially increases and then decreases as β_1 values increase and reaches a maximum when $\beta_1 = 1e - 3$ under both datasets. The PNSR value curve remains stable on the CAVET dataset while having an anomalous spike on the PaviaU dataset

in Fig. 9(e). Subsequent experiments reveal that the algorithm fails to converge with $\beta_2 = 0.1$ on the PaviaU dataset. To obtain the best reconstruction results, β_1 and β_2 are set to $1e - 3$ and 1 in all experiments.

3) *TR ranks* r: TNN imposes constraints on the TR factors to capture more low-rank prior and enhance the robustness of the TR ranks $r = [r_1, r_2, r_2]$. The range of the TR rank is set according to [22] and [43]. As shown in Fig. 9(f)–(h), the curves of PSNR values variation with TR ranks on all three datasets at 0.1 sampling ratio verify the robustness. The PSNR values increase with increasing values of r_1 and r_2 until $r_1 = 9$ and $r_2 = 3$, then gradually decrease or stabilize on all datasets. It suggests that the setting of TR ranks is robust, and the TNN regularization is effective. TR ranks are set to $[9, 3, 3]^T$ in each reconstruction experiment.

3) Convergence Analysis: The proposed algorithm consists of two iterations, the inner and the outer. The inner one focuses on the iteration of the ADMM algorithm. The outer iteration focuses on updating the subspace and provides initial values for the inner iteration. Fig. 10 plots the convergence curves on the PaviaU dataset at the sampling ratio of 0.05. The overall decreasing curve of the relative change in $\mathcal{X}$ eventually converges to 0, indicating that our algorithm is converged in both inner and outer iterations.

4) HSI-CSR in Noise Case: The captured real HSI data usually contains the noise. To evaluate the CS reconstruction performance of the proposed method in noisy case, additive Gaussian independent and identically distributed noise is added to each band of HSI, with the variances of 0.1 and 0.05. Table IV presents the qualitative results for experimental models with different levels of noise on the PaviaU dataset under sr = 0.1, and the optimal evaluation indicators are indicated in bold. As the variances increase, the noise in the original HSI is enhanced and the CS reconstruction quality deteriorates. From Table IV, all the comparison models resist part of the noise interference, the proposed SQV-AwTR achieves the best reconstruction results in all noisy case, indicating the superiority and robustness of the proposed model.

V. CONCLUSION

In this article, a novel subspace-based model for HSI-CSR that simultaneously constrains the spectral basis and feature HSI is proposed to capture global low-rankness and spectral smoothness. The proposed model utilizes spectral quadratic variation to substitute the orthogonal constraint, enhancing the spectral continuity and reducing the spectral distortion. TNN is applied to the TR factors decomposed from the feature HSI and improves the low-rank approximation compared to single TR decomposition. Moreover, the optimization process ensures the robustness of setting TR ranks. An autoweighted strategy is employed to characterize the different contributions of different TR factors to low-rank decomposition and enhance the reconstructed quality. The results of numerical and ablation experiments confirm the effectiveness of the proposed model, particularly at small sampling ratios. In the future, nonlocal self-similarity can be integrated into the framework to enhance

TABLE IV
Quantitative Results for Experimental Models With Different Levels of Noise on the PaviaU Dataset Under sr=0.1

Variances	Index	Noisy	DCT	LRTV	JTenRe3-DTV	$l_0 - l_1$HTV	GNLR	NGMeet	SQV-AwTR
0.1	PSNR	19.996	25.177	25.489	26.898	29.021	25.802	28.774	**34.068**
	SSIM	0.3672	0.5960	0.6468	0.6666	0.8248	0.6133	0.8283	**0.9045**
	ERGAS	376.61	211.06	202.06	109.80	132.81	192.73	135.99	**70.96**
0.05	PSNR	26.019	27.181	29.755	30.887	31.983	30.1154	33.5828	**38.945**
	SSIM	0.6357	0.7013	0.8407	0.8479	0.8925	0.7998	0.9141	**0.9514**
	ERGAS	188.32	165.04	123.92	107.79	95.1913	118.06	79.73	**49.20**

reconstruction efficiency. Furthermore, exploring the application of the proposed model for snapshot compressive HSI or HSI denoising presents avenues for future research.

ACKNOWLEDGMENT

REFERENCES

[1] D. L. Donoho, "Compressed sensing," *IEEE Trans. Inf. Theory*, vol. 52, no. 4, pp. 1289–1306, Apr. 2006.

[2] E. J. Candès et al., "Compressive sampling," in *Proc. Int. Congr. Mathematicians*, 2006, vol. 3, pp. 1433–1452.

[3] C. Li, T. Sun, K. F. Kelly, and Y. Zhang, "A compressive sensing and unmixing scheme for hyperspectral data processing," *IEEE Trans. Image Process.*, vol. 21, no. 3, pp. 1200–1210, Mar. 2012.

[4] Y. Xu, Z. Wu, J. Chanussot, and Z. Wei, "Joint reconstruction and anomaly detection from compressive hyperspectral images using Mahalanobis distance-regularized tensor RPCA," *IEEE Trans. Geosci. Remote Sens.*, vol. 56, no. 5, pp. 2919–2930, May 2018.

[5] X. Yuan, D. J. Brady, and A. K. Katsaggelos, "Snapshot compressive imaging: Theory, algorithms, and applications," *IEEE Signal Process. Mag.*, vol. 38, no. 2, pp. 65–88, Mar. 2021.

[6] Y. Li, F. Dai, X. Cheng, L. Xu, and G. Gui, "Multiple-prespecified-dictionary sparse representation for compressive sensing image reconstruction with nonconvex regularization," *J. Franklin Inst.*, vol. 356, no. 4, pp. 2353–2371, 2019.

[7] L. Wang, Z. Xiong, G. Shi, F. Wu, and W. Zeng, "Adaptive nonlocal sparse representation for dual-camera compressive hyperspectral imaging," *IEEE Trans. Pattern Anal. Mach. Intell.*, vol. 39, no. 10, pp. 2104–2111, Oct. 2017.

[8] Y. Liu, X. Yuan, J. Suo, D. J. Brady, and Q. Dai, "Rank minimization for snapshot compressive imaging," *IEEE Trans. Pattern Anal. Mach. Intell.*, vol. 41, no. 12, pp. 2990–3006, Dec. 2019.

[9] C. Li, L. Ma, Q. Wang, Y. Zhou, and N. Wang, "Construction of sparse basis by dictionary training for compressive sensing hyperspectral imaging," in *Proc. IEEE Int. Geosci. Remote Sens. Symp.*, 2013, pp. 1442–1445.

[10] X. Lin, Y. Liu, J. Wu, and Q. Dai, "Spatial-spectral encoded compressive hyperspectral imaging," *ACM Trans. Graph.*, vol. 33, no. 6, Nov. 2014, Art. no. 233, doi: 10.1145/2661229.2661262.

[11] D. Needell and R. Ward, "Near-optimal compressed sensing guarantees for total variation minimization," *IEEE Trans. Image Process.*, vol. 22, no. 10, pp. 3941–3949, Oct. 2013.

[12] P. Meza, I. Ortiz, E. Vera, and J. Martinez, "Compressive hyperspectral imaging recovery by spatial-spectral non-local means regularization," *Opt. Exp.*, vol. 26, no. 6, pp. 7043–7055, 2018.

[13] M. Wang, Q. Wang, J. Chanussot, and D. Hong, "L_0-L_1 hybrid total variation regularization and its applications on hyperspectral image mixed noise removal and compressed sensing," *IEEE Trans. Geosci. Remote Sens.*, vol. 59, no. 9, pp. 7695–7710, Sep. 2021.

[14] W. Chen, "Simultaneously sparse and low-rank matrix reconstruction via nonconvex and nonseparable regularization," *IEEE Trans. Signal Process.*, vol. 66, no. 20, pp. 5313–5323, Oct. 2018.

[15] J. Xue, Y. Zhao, W. Liao, and J. C.-W. Chan, "Hyper-Laplacian regularized nonlocal low-rank matrix recovery for hyperspectral image compressive sensing reconstruction," *Inf. Sci.*, vol. 501, pp. 406–420, 2019. [Online]. Available: https://www.sciencedirect.com/science/article/pii/S0020025519305511

[16] H. Vargas and H. Arguello, "A low-rank model for compressive spectral image classification," *IEEE Trans. Geosci. Remote Sens.*, vol. 57, no. 12, pp. 9888–9899, Dec. 2019.

[17] X. Wang, L. T. Yang, L. Kuang, X. Liu, Q. Zhang, and M. J. Deen, "A tensor-based big-data-driven routing recommendation approach for heterogeneous networks," *IEEE Netw.*, vol. 33, no. 1, pp. 64–69, Jan./Feb. 2019.

[18] X. Wang, L. T. Yang, L. Song, H. Wang, L. Ren, and M. J. Deen, "A tensor-based multiattributes visual feature recognition method for industrial intelligence," *IEEE Trans. Ind. Inform.*, vol. 17, no. 3, pp. 2231–2241, Mar. 2021.

[19] M. Wang et al., "Tensor decompositions for hyperspectral data processing in remote sensing: A comprehensive review," *IEEE Geosci. Remote Sens. Mag.*, vol. 11, no. 1, pp. 26–72, Mar. 2023.

[20] S. Das, "Hyperspectral image, video compression using sparse tucker tensor decomposition," *IET Image Process.*, vol. 15, no. 4, pp. 964–973, 2021. [Online]. Available: https://ietresearch.onlinelibrary.wiley.com/doi/abs/10.1049/ipr2.12077

[21] Y. Wang, L. Lin, Q. Zhao, T. Yue, D. Meng, and Y. Leung, "Compressive sensing of hyperspectral images via joint tensor tucker decomposition and weighted total variation regularization," *IEEE Geosci. Remote Sens. Lett.*, vol. 14, no. 12, pp. 2457–2461, Dec. 2017.

[22] Y. Chen, T.-Z. Huang, W. He, N. Yokoya, and X.-L. Zhao, "Hyperspectral image compressive sensing reconstruction using subspace-based nonlocal tensor ring decomposition," *IEEE Trans. Image Process.*, vol. 29, pp. 6813–6828, 2020.

[23] Q. Zhao, G. Zhou, S. Xie, L. Zhang, and A. Cichocki, "Tensor ring decomposition," 2016. [Online]. Available: http://arxiv.org/abs/1606.05535

[24] O. Mickelin and S. Karaman, "On algorithms for and computing with the tensor ring decomposition," *Numer. Linear Algebra with Appl.*, vol. 27, no. 3, 2020, Art. no. e2289. [Online]. Available: https://onlinelibrary.wiley.com/doi/abs/10.1002/nla.2289

[25] Z. Zhang, G. Ely, S. Aeron, N. Hao, and M. Kilmer, "Novel methods for multilinear data completion and de-noising based on tensor-SVD," in *Proc. IEEE Conf. Comput. Vis. Pattern Recognit.*, 2014, pp. 3842–3849.

[26] C. Lu, J. Feng, Y. Chen, W. Liu, Z. Lin, and S. Yan, "Tensor robust principal component analysis with a new tensor nuclear norm," *IEEE Trans. Pattern Anal. Mach. Intell.*, vol. 42, no. 4, pp. 925–938, Apr. 2020.

[27] H. Fan, Y. Chen, Y. Guo, H. Zhang, and G. Kuang, "Hyperspectral image restoration using low-rank tensor recovery," *IEEE J. Sel. Topics Appl. Earth Observ. Remote Sens.*, vol. 10, no. 10, pp. 4589–4604, Oct. 2017.

[28] H. Li, X.-L. Zhao, J. Lin, and Y. Chen, "Low-rank tensor optimization with nonlocal plug-and-play regularizers for snapshot compressive imaging," *IEEE J. Sel. Topics Appl. Earth Observ. Remote Sens.*, vol. 15, pp. 581–593, 2022.

[29] Y.-B. Zheng, T.-Z. Huang, X.-L. Zhao, T.-X. Jiang, T.-H. Ma, and T.-Y. Ji, "Mixed noise removal in hyperspectral image via low-fibered-rank regularization," *IEEE Trans. Geosci. Remote Sens.*, vol. 58, no. 1, pp. 734–749, Jan. 2020.

[30] M. Wang, Q. Wang, J. Chanussot, and D. Hong, "Total variation regularized weighted tensor ring decomposition for missing data recovery in high-dimensional optical remote sensing images," *IEEE Geosci. Remote Sens. Lett.*, vol. 19, 2022, Art. no. 6002505.

[31] J. Xue, Y. Zhao, W. Liao, J. C.-W. Chan, and S. G. Kong, "Multilayer sparsity-based tensor decomposition for low-rank tensor completion," *IEEE Trans. Neural Netw. Learn. Syst.*, vol. 33, no. 11, pp. 6916–6930, Nov. 2022.

[32] H. Zeng, J. Xue, H. Q. Luong, and W. Philips, "Multimodal core tensor factorization and its applications to low-rank tensor completion," *IEEE Trans. Multimedia*, vol. 25, pp. 7010–7024, 2023.

[33] W. He et al., "Non-local meets global: An iterative paradigm for hyperspectral image restoration," *IEEE Trans. Pattern Anal. Mach. Intell.*, vol. 44, no. 4, pp. 2089–2107, Apr. 2022.

[34] J. Peng, Q. Xie, Q. Zhao, Y. Wang, L. Yee, and D. Meng, "Enhanced 3DTV regularization and its applications on HSI denoising and compressed sensing," *IEEE Trans. Image Process.*, vol. 29, pp. 7889–7903, 2020.

[35] Y. Chen, W. He, X.-L. Zhao, T.-Z. Huang, J. Zeng, and H. Lin, "Exploring nonlocal group sparsity under transform learning for hyperspectral image denoising," *IEEE Trans. Geosci. Remote Sens.*, vol. 60, 2022, Art. no. 5537518.

[36] L. Sun, B. Jeon, Z. Wu, and L. Xiao, "Hyperspectral denoising via cross total variation-regularized unidirectional nonlocal low-rank tensor approximation," in *Proc. 25th IEEE Int. Conf. Image Process.*, 2018, pp. 2900–2904.

[37] L. Sun, C. He, Y. Zheng, Z. Wu, and B. Jeon, "Tensor cascaded-rank minimization in subspace: A unified regime for hyperspectral image low-level vision," *IEEE Trans. Image Process.*, vol. 32, pp. 100–115, 2023.

[38] T. G. Kolda and B. W. Bader, "Tensor decompositions and applications," *SIAM Rev.*, vol. 51, no. 3, pp. 455–500, 2009, doi: 10.1137/07070111X.

[39] T. Yokota, Q. Zhao, and A. Cichocki, "Smooth PARAFAC decomposition for tensor completion," *IEEE Trans. Signal Process.*, vol. 64, no. 20, pp. 5423–5436, Oct. 2016.

[40] Y. Xu, Z. Wu, J. Chanussot, and Z. Wei, "Hyperspectral computational imaging via collaborative tucker3 tensor decomposition," *IEEE Trans. Circuits Syst. Video Technol.*, vol. 31, no. 1, pp. 98–111, Jan. 2021.

[41] W. He, N. Yokoya, L. Yuan, and Q. Zhao, "Remote sensing image reconstruction using tensor ring completion and total variation," *IEEE Trans. Geosci. Remote Sens.*, vol. 57, no. 11, pp. 8998–9009, Nov. 2019.

[42] I. V. Oseledets, "Tensor-train decomposition," *SIAM J. Sci. Comput.*, vol. 33, no. 5, pp. 2295–2317, 2011, doi: 10.1137/090752286.

[43] Y. Chen, W. He, N. Yokoya, T.-Z. Huang, and X.-L. Zhao, "Nonlocal tensor-ring decomposition for hyperspectral image denoising," *IEEE Trans. Geosci. Remote Sens.*, vol. 58, no. 2, pp. 1348–1362, Feb. 2020.

[44] W. He, Y. Chen, N. Yokoya, C. Li, and Q. Zhao, "Hyperspectral super-resolution via coupled tensor ring factorization," *Pattern Recognit.*, vol. 122, 2022, Art. no. 108280. [Online]. Available: https://www.sciencedirect.com/science/article/pii/S003132032100460X

[45] L. Yuan, C. Li, D. Mandic, J. Cao, and Q. Zhao, "Tensor ring decomposition with rank minimization on latent space: An efficient approach for tensor completion," in *Proc. 33rd AAAI Conf. Artif. Intell., 31st Innov. Appl. Artif. Intell. Conf., 9th AAAI Symp. Educ. Adv. Artif. Intell.*, 2019, pp. 9151–9158, doi: 10.1609/aaai.v33i01.33019151.

[46] X. Luo, J. Lv, B. Wang, D. Liu, and J. Wang, "Hyperspectral image restoration via hybrid smoothness regularized auto-weighted low-rank tensor ring factorization," *Front. Earth Sci.*, vol. 10, 2023, Art. no. 1022874. [Online]. Available: https://www.frontiersin.org/articles/10.3389/feart.2022.1022874

[47] C. Chen, H. Qian, W. Chen, Z. Zheng, and H. Zhu, "Auto-weighted multiview constrained spectral clustering," *Neurocomputing*, vol. 366, pp. 1–11, 2019. [Online]. Available: https://www.sciencedirect.com/science/article/pii/S0925231219310227

[48] H. Xu, M. Qin, S. Chen, Y. Zheng, and J. Zheng, "Hyperspectral-multispectral image fusion via tensor ring and subspace decompositions," *IEEE J. Sel. Topics Appl. Earth Observ. Remote Sens.*, vol. 14, pp. 8823–8837, 2021.

[49] G. Golub, S. Nash, and C. Van Loan, "A Hessenberg-Schur method for the problem AX + XB= C," *IEEE Trans. Autom. Control*, vol. 24, no. 6, pp. 909–913, Dec. 1979.

[50] J. M. Bioucas-Dias and J. M. P. Nascimento, "Hyperspectral subspace identification," *IEEE Trans. Geosci. Remote Sens.*, vol. 46, no. 8, pp. 2435–2445, Aug. 2008.

[51] W. He, H. Zhang, L. Zhang, and H. Shen, "Total-variation-regularized low-rank matrix factorization for hyperspectral image restoration," *IEEE Trans. Geosci. Remote Sens.*, vol. 54, no. 1, pp. 178–188, Jan. 2016.

Dan Li received the B.S., M.S., and Ph.D. degrees in control science and engineering from the Harbin Institute of Technology, Harbin, China, in 2012, 2014, and 2018, respectively.

She is currently an Associate Professor with the College of Astronautics, Nanjing University of Aeronautics and Astronautics, Nanjing, China. Her research interests include hyperspectral image classification, signal processing, sparse sampling, and reconstruction technology.

Fanqiang Kong received the Ph.D. degree in information and communication engineering from Xidian University, Xi'an, China, in 2008.

He is currently a Professor with the College of Astronautics, Nanjing University of Aeronautics and Astronautics, Nanjing, China. His research interests include spectral image coding and image analysis, artificial intelligence, and pattern recognition.

Yanyan Lv received the B.S. degree in optoelectronic information science and engineering from the Nanjing University of Aeronautics and Astronautics, Nanjing, China, in 2023, where she is currently working toward the master's in optical engineering degree.

Her research interests include hyperspectral image processing, compressive sensing, low-rank representation, and sparse optimization.

Xinwei Wan received the B.S. degree in control science and engineering from Southeast University, Nanjing, China, in 2021, and the M.S. degree in electronic information from the Nanjing University of Aeronautics and Astronautics, Nanjing, in 2024.

Her research interests include hyperspectral image reconstruction and compressive sensing.
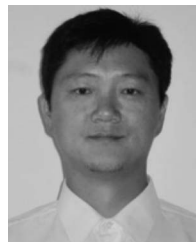
Qiang Wang (Member, IEEE) received the B.S., M.S., and Ph.D. degrees in control science and engineering from the Harbin Institute of Technology (HIT), Harbin, China, in 1998, 2000, and 2004, respectively.

Since 2008, he has been a Professor with the Department of Control Science and Engineering, HIT. His research interests include signal/image processing, multisensor data fusion, wireless sensor networks, and intelligent detection technology.